Numerical study on the effects of non-dimensional parameters on drop-on-demand droplet formation dynamics and printability range in the up-scaled model

Eunjeong Kim and Jehyun Baek

Citation: Physics of Fluids (1994-present) **24**, 082103 (2012); doi: 10.1063/1.4742913
View online: http://dx.doi.org/10.1063/1.4742913
View Table of Contents: http://scitation.aip.org/content/aip/journal/pof2/24/8?ver=pdfcov
Published by the AIP Publishing

Numerical study on the effects of non-dimensional parameters on drop-on-demand droplet formation dynamics and printability range in the up-scaled model

Eunjeong Kim and Jehyun Baek[a)]
Department of Mechanical Engineering, POSTECH, San 31, Hyoja-dong, Pohang 790-784, South Korea

(Received 17 April 2012; accepted 9 July 2012; published online 14 August 2012)

The droplet formation dynamics from a drop-on-demand printhead is numerically investigated with regard to the printability range. The numerical simulation is carried out using a volume-of-fluid model, and the qualitative effects of non-dimensional parameters on the droplet formation dynamics are evaluated. To determine the printability range, within which the droplet is ejected in a stable manner without satellite droplets, extensive numerical simulations are carried out by varying the viscosity and surface tension. Generally, the printability range is determined by a Z number, which is the inverse of the Ohnesorge number (Oh). However, it is found that the Z number alone is insufficient for describing the droplet formation dynamics. Other important non-dimensional parameters such as the Reynolds number (Re), Weber number (We), and capillary number (Ca) should also be taken into consideration. For studying the printability, the droplet formation dynamics are divided into five different regimes, and a regime map based on the Z, We, and Ca is proposed. © *2012 American Institute of Physics*. [http://dx.doi.org/10.1063/1.4742913]

I. INTRODUCTION

In recent years, inkjet printing technology has gained a lot of popularity as a versatile technique for fabricating flexible displays, electronic circuits, polymeric coatings, thin films,[1] small ceramic parts, MEMS components,[2] and optical devices such as microlenses.[3] Inkjet printing is highly advantageous for such applications owing to its inexpensive, efficient, and simple process.

There are two main types of inkjet printheads: a continuous inkjet printhead and a drop-on-demand (DOD) printhead. In the former type, a continuous stream of droplets is formed by Rayleigh instability, whereas in the latter type, a droplet is ejected when an actuation pulse is applied. The DOD printhead is preferred in inkjet printers because of its simplicity and the feasibility of decreasing the size of the system.[4] Therefore, the present study focuses on droplet formation in the DOD mode.

Many researchers have studied droplet formations in the DOD mode by using experimental[5–11] and numerical methods.[12–19] A typical process of DOD droplet formation consists of several stages: the ejection and stretching of the liquid, pinch-off of the liquid thread from the nozzle exit, contraction of the liquid thread, breakup of the liquid thread into primary and satellite droplets, recombination of the primary and satellite droplets, and droplet oscillation to equilibrium state.[6] Castrejón-Pita *et al.* presented a simple experimental device, which can produce droplets on demand or in a continuous mode, and provided a large-scale model for real inkjet printing system.[8] Feng[16] carried out simulation with fluid dynamics package, Flow 3D, and the effects of the incoming flow rate and duration of the square pulse wave were considered. Xu and Basaran[18] carried out a computational analysis of DOD droplet formation, and they found three regimes of operation. When Weber number is low, breakup does not occur, and when it is large enough to cause pinch-off, droplets are formed but they

[a)]Author to whom correspondence should be addressed. Electronic mail: jhbaek@postech.ac.kr.

might have negative or positive velocities depending on the Weber number. Droplet with negative velocity is undesirable because it may move toward the nozzle. The effects of driving waveform on the DOD droplet formation dynamics have been investigated by Chen and Basaran,[5] Kwon,[9] Liou *et al.*[19] Particular effort also has been dedicated to produce droplets smaller than the nozzle diameter.[5,7] A detailed review on the inkjet printing is given by Wijshoff.[20] In addition to studies of Newtonian fluids, there have been several studies on DOD droplet formation using non-Newtonian fluids, which are generally used in many industrial applications. Morrison and Harlen[21] investigated the effects of viscoelasticity on DOD droplet formation via numerical simulations. They found that satellite droplets can potentially be eliminated by adding polymer to the ink; however, elasticity can also reduce the droplet velocity and can delay or even prevent the pinch-off of the droplets from the nozzle. They also proposed a two-dimensional map of characteristic jet types in terms of the viscoelastic parameters.

In inkjet printing technology, the main aim is to generate stable droplets without the formation of satellite droplets, which adversely affects the printing quality. To achieve stable droplet generation, the printability of ink is of great importance, and it has been extensively studied.[12,15,22–25] These studies evaluated the printability of ink in terms of the Z number, which is the inverse of the Ohnesorge number. Fromm[12] solved the Navier–Stokes equation in terms of non-dimensional parameters, and he found that stable droplet formation was possible in DOD systems when $Z > 2$. In other literatures, the printable range was found to be 1–10[23,24,26] and 4–14,[25] depending on the combination of the printhead and ink used. When the value of Z is less than the lower limit of Z, the fluid inertia is insufficient for overcoming the viscous force, and as a result, no droplet is formed. When the value of Z is more than the upper limit of Z, a satellite droplet is formed.[26] Derby[22] provided a detailed review on the printability range, and Derby and Reis[23] provided a map defining a region of the parameter space of Weber and Reynolds number, within which DOD inkjet printing is possible considering additional two limits to practical droplet generation: a minimum value of Weber number to overcome surface tension which resists droplet ejection and the critical threshold to avoid the splashing after droplet impact onto a substrate. However, a detailed study on printability is still inadequate.

We focused on examining the qualitative effects of non-dimensional parameters on droplet formation dynamics; we also focused on determining the printability range for Newtonian fluids. In this study, we employed a numerical simulation method for examining these effects because it allows the independent and systematic control of various parameters. Numerical simulations were carried out under a wide range of jetting conditions, and the qualitative effects of non-dimensional parameters on the droplet formation dynamics were evaluated. The volume and speed of the ejected droplets are also important parameters to be considered when determining the printing quality. However, in this study, we only focused on the printability range. To determine the printability range, Jang *et al.*[25] considered single droplet formation, positional accuracy, and maximum allowable jetting frequency, but we only considered single droplet formation because printing inaccuracy is mainly caused by satellite droplets (Link and Semiat, 2009).[27]

II. NUMERICAL METHOD

A. Governing equations

Numerical simulations were carried out using the commercial computational fluid dynamics package, Fluent 6.3. The axisymmetric time-dependent governing equations for continuity and momentum were solved.

Continuity equation:

$$\frac{\partial \rho}{\partial t} + \nabla \cdot (\rho \vec{v}) = 0, \tag{1}$$

Momentum equation:

$$\frac{\partial}{\partial t}(\rho \vec{v}) + \nabla \cdot (\rho \vec{v} \vec{v}) = -\nabla p + \nabla \cdot \left[\mu \left(\nabla \vec{v} + \nabla \vec{v}^T\right)\right] + \rho \vec{g} + \vec{F}, \tag{2}$$

where $\vec{v}$ is the velocity vector, p is the pressure, $\vec{g}$ is the gravitational acceleration, μ is the viscosity, and $\vec{F}$ is the surface tension force per unit volume.

The volume-of-fluid (VOF) model[28] was used for tracking the gas-liquid interface; the tracking of the interface was achieved by solving the volume fraction equation, which is given by

$$\frac{\partial \alpha_G}{\partial t} + \vec{v} \cdot \nabla \alpha_G = 0, \tag{3}$$

where α_G is the volume fraction of the gas phase.

The density and viscosity in the VOF model are given by

$$\rho = \alpha_G \rho_G + (1 - \alpha_G)\rho_L, \tag{4}$$

$$\mu = \alpha_G \mu_G + (1 - \alpha_G)\mu_L. \tag{5}$$

The subscripts G and L represent the gas and liquid phases, respectively. The surface tension force $\vec{F}$ in Eq. (2) was modeled using the continuum surface force model;[29] the equation of surface tension force $\vec{F}$ is given as follows:

$$\vec{F} = \sigma \frac{\rho \kappa \nabla \alpha_G}{\frac{1}{2}(\rho_L + \rho_G)}, \tag{6}$$

where κ is the curvature of the gas–liquid interface, which is calculated as

$$\kappa = -(\nabla \cdot \hat{n}), \tag{7}$$

where the unit vector $\hat{n}$ normal to the interface is given by

$$\hat{n} = \frac{\nabla \alpha_G}{|\nabla \alpha_G|}. \tag{8}$$

The contact angle θ, which represents the wetting properties of the wall, was used to calculate the unit normal to the interface at the cell next to the wall, given by

$$\hat{n} = \hat{n}_w \cos\theta + \hat{t}_w \sin\theta, \tag{9}$$

where $\hat{n}_w$ and $\hat{t}_w$ are the unit vectors normal and tangential to the wall, respectively.

The pressure implicit with splitting of operators scheme was used for the pressure-velocity coupling. The pressure staggering option scheme and second-order upwind scheme were used for interpolating the pressure and momentum equations, respectively. The geo-reconstruct scheme was used for reconstructing the interface. A variable time-stepping method, in which the time step was calculated for a fixed value of the Courant number (0.2), was used for reducing the calculation time.

The three independent non-dimensional parameters are the Reynolds number *Re*, Weber number *We*, and Bond number *Bo*:

$$\mathrm{Re} = \frac{Inertial\ effects}{Viscous\ effects} = \frac{\rho V R}{\mu}, \tag{10}$$

$$We = \frac{Inertial\ effects}{Capillary\ effects} = \frac{\rho V^2 R}{\sigma}, \tag{11}$$

$$Bo = \frac{Gravity\ effects}{Capillary\ effects} = \frac{\rho g R^2}{\sigma}, \tag{12}$$

where R is the nozzle radius (m), V is the velocity scale of the droplet ejection process (ms^{-1}), σ is the surface tension ($\mathrm{N\ m}^{-1}$), and ρ is the density ($\mathrm{kg\ m}^{-3}$). Another relevant non-dimensional parameter is the capillary number $Ca = We/Re$, which is the ratio of the viscous force to the capillary force. Another important non-dimensional parameter for determining the printability range is the Z number, $Z = Re/We^{1/2} = (R\rho\sigma)^{1/2}/\mu$ (inverse of the Ohnesorge number), which is determined only by the fluid properties, irrespective of the velocity scale of the system.

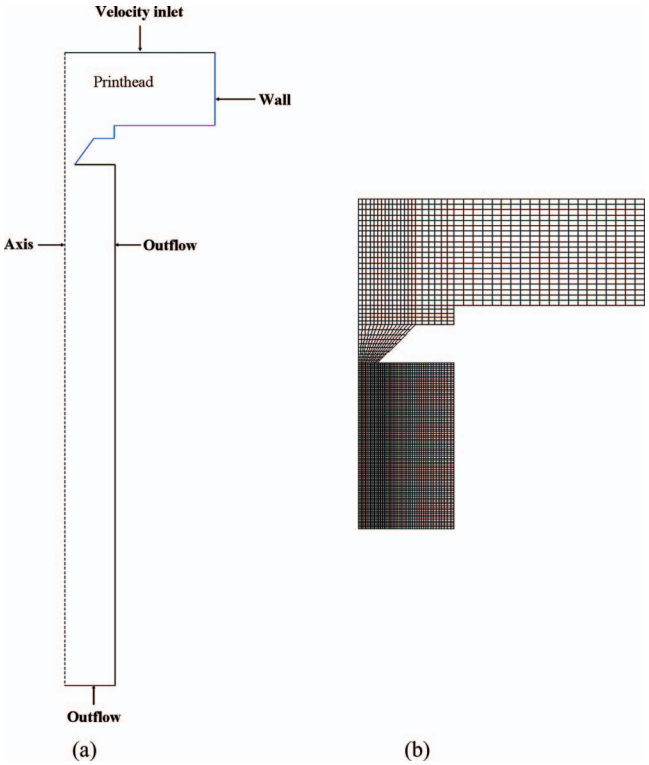

FIG. 1. (a) Schematic diagram showing the 2D axisymmetric computational domain and boundary conditions, and (b) computational mesh generation.

B. Boundary conditions

The geometry of the printhead and shape of the actuation pulse used in this study are identical to those used in the experiments of Castrejón-Pita *et al.*[30] They presented a large-scale model for real inkjet printing systems, which have a much larger nozzle than those used in practical applications. However, they carefully chose the jetting parameters to match the non-dimensional parameters (*Re* and *We*) of a generic commercial DOD printhead, for which the nozzle diameter is typically 50 μm and the droplet speed is $\sim$6 ms^{-1}. It should be noted that the large-scale model does not exactly match the dynamics of a commercial printhead because of gravity, which has a relatively stronger effect when the nozzle diameter is increased.[30]

The printhead domain is shown in Fig. 1; the height of the printhead domain and radius of the flow inlet are 8.6 and 15 mm, respectively. The nozzle radius is 1 mm. The height and radius of the rectangular area below the printhead are 40 and 5 mm, respectively. A no-slip condition was imposed on the wall inside the printhead, and a static contact angle on the wall is assumed as 10° in order to pin the contact line at the edge of the nozzle outlet.[30] A mesh with 23 075 cells was found to yield mesh-independent results; this mesh was chosen for the simulations. At the inlet of the printhead, an actuation pulse was applied in terms of the variation in velocity according to the boundary condition used in Lagrangian simulations of Castrejón-Pita *et al.*,[30] as shown in Fig. 2(a).

To validate the results of the VOF simulation, DOD droplet formation for a glycerol-water mixture was simulated and compared with the results obtained by Castrejón-Pita *et al.*[30] The density, viscosity, and surface tension of the glycerol-water mixture are 1222 Kg m^{-3}, 0.1 Kg m^{-1}s^{-1}, and 0.064 N m^{-1}, respectively.

To examine the qualitative effects of the non-dimensional parameters on the droplet formation dynamics, we carried out extensive numerical simulations over the ranges $0.7 \leq Z \leq 14.0$, $1.4 \leq Re \leq 40.8$, $0.6 \leq We \leq 12$, and $Bo \leq 0.24$. The nozzle used in the present study was much larger than nozzles used in practical applications; however, the values of *Z*, *Re*, and *We* were within the typical ranges of non-dimensional values for microscale inkjet printing. A small *Bo* number implies that the

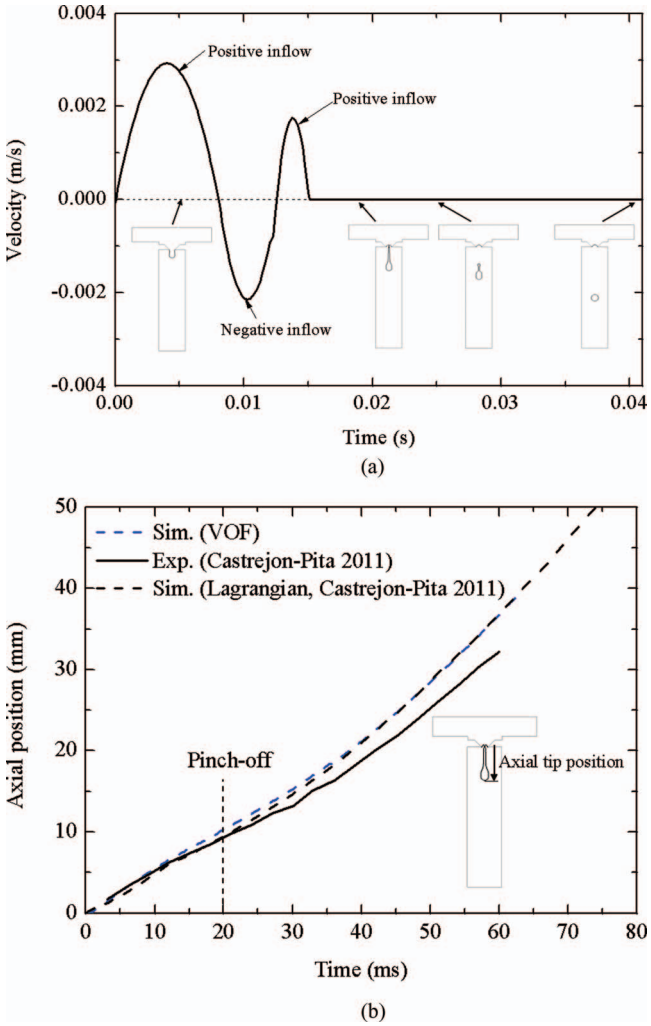

FIG. 2. (a) Scaled ($\alpha = 0.084$) inlet velocity $V(t)$ obtained by a parabolic fitting to the inlet condition used in Lagrangian simulation of Castrejón–Pita *et al.*[30] The insets show the shape evolutions of droplets obtained by the present numerical simulation ($t = 6.1$, 18.2, 25.3, and 40.4 ms). (b) Comparison of numerical results of VOF method with experimental and Lagrangian simulation results of Castrejón–Pita *et al.*,[30] in terms of axial tip position.

gravity effects are insignificant compared to the capillary effects; thus, the influence of gravity was not discussed in the present study.

In the numerical simulations, viscosity and surface tension were varied under a fixed density, nozzle radius, and actuation pulse. Therefore, the non-dimensional parameters scaled as $Z \sim \sigma^{1/2}/\mu$, $Re \sim 1/\mu$, $We \sim 1/\sigma$, and $Ca \sim \mu/\sigma$. The values of viscosity and surface tension were varied while the ratio of $\sigma^{1/2}/\mu$ was kept constant. In turn, the value of Z was maintained constant, and the values of Re, We, and Ca were varied; these values are listed in Tables I and II (Tables I and II present only some of the jetting conditions that were simulated in this study). Through these numerical experiments set, the influence of Re, We, and Ca on the droplet formation dynamics at a fixed Z number was evaluated.

III. NUMERICAL RESULTS

A. Qualitative effects of non-dimensional parameters on droplet formation dynamics

To validate the numerical model, the numerical results were compared with results obtained by Castrejón-Pita *et al.*[30] through experiments and Lagrangian simulations. Figure 2(a) shows the time

TABLE I. Fluid properties and non-dimensional parameters at $Z = 11.8$.

μ (Kg m^{-1}s^{-1})	σ (N m^{-1})	Z	Re	We	Ca
0.015	0.03	11.8	40.7	12.0	0.29
0.017	0.04	11.8	35.3	9.0	0.25
0.019	0.05	11.8	31.6	7.2	0.23
0.022	0.07	11.8	26.8	5.1	0.19
0.026	0.09	11.8	23.5	4.0	0.17
0.033	0.15	11.8	18.2	2.4	0.13
0.066	0.60	11.8	9.2	0.6	0.06

evolution of the droplet shape, and our numerical results closely reproduced the droplet formation process (see Fig. 10 in Castrejón-Pita *et al.*[30]). Figure 2(b) shows a good agreement between the axial tip positions obtained by the present numerical simulation and that obtained by the experimental results, up to pinch-off (20 ms). During the free flight of the droplet after pinch-off, both the present VOF-based simulation and the Lagrangian simulation slightly overpredicted the axial tip position. The deviation could be explained by slight differences in the velocity condition at the printhead inlet between the experiment and simulation. The velocity variation (negative inflow) after 15 ms up to pinch-off (see Fig. 8 in Castrejón-Pita *et al.*[30]), which may locally affect the tail of the liquid thread by pulling the tail toward the nozzle and consequently leading to a decrease in the forward momentum of tail tip, was neglected in the simulations. The neglect of negative inflow after 15 ms in the simulations could result in overestimated forward momentum, in turn, might result in overestimated forward momentum of droplet after the tail was fully absorbed into the head, and consequently result in slightly overestimated falling velocity compared to the experiment. Through these comparisons, it can be concluded that the numerical simulations carried out using the VOF method were reasonably accurate for predicting the droplet formation process in DOD devices, though not exact. During the first positive inflow (up to 8 ms), the fluid in the nozzle is accelerated and pushed out of the nozzle, as shown in Fig. 2(a). When the inflow is negative (from 8 to 12 ms), the liquid thread is pulled back into the nozzle, promoting its separation from the nozzle; nevertheless, the axial tip position of the droplet continues to move forward because of inertia.[18] During the second positive inflow (from 12 to 15 ms), forward momentum is applied again. When the liquid thread pinches off from the nozzle exit, it has a tail and a round head. Then, the tail recoils toward the head owing to high pressure in the tail tip,[6] forming a single spherical droplet.

Prior to determining the printability range, numerical simulations of the droplet formation under a wide range of jetting conditions were carried out and the qualitative effects of non-dimensional parameters on the droplet formation dynamics were examined.

1. Ejection and stretching of liquid thread before pinch-off

Figures 3(a) and 3(b) show the time evolution of the axial tip position up to pinch-off at $Z = 11.8$ and $Z = 1$, respectively. It can be seen that the ejection speed during the initial stage (up to 4 ms) of the first positive inflow is not influenced by viscosity and surface tension. It appears that the ejection speed during the initial stage is determined only by the magnitude of the actuation pulse,

TABLE II. Fluid properties and non-dimensional parameters at $Z = 1.0$.

μ (Kg m^{-1}s^{-1})	σ (N m^{-1})	Z	Re	We	Ca
0.17	0.03	1.0	3.5	12.0	3.4
0.20	0.04	1.0	3.0	9.0	3.0
0.22	0.05	1.0	2.7	7.2	2.6
0.26	0.07	1.0	2.3	5.1	2.2
0.30	0.09	1.0	2.0	4.0	2.0
0.38	0.15	1.0	1.6	2.4	1.5

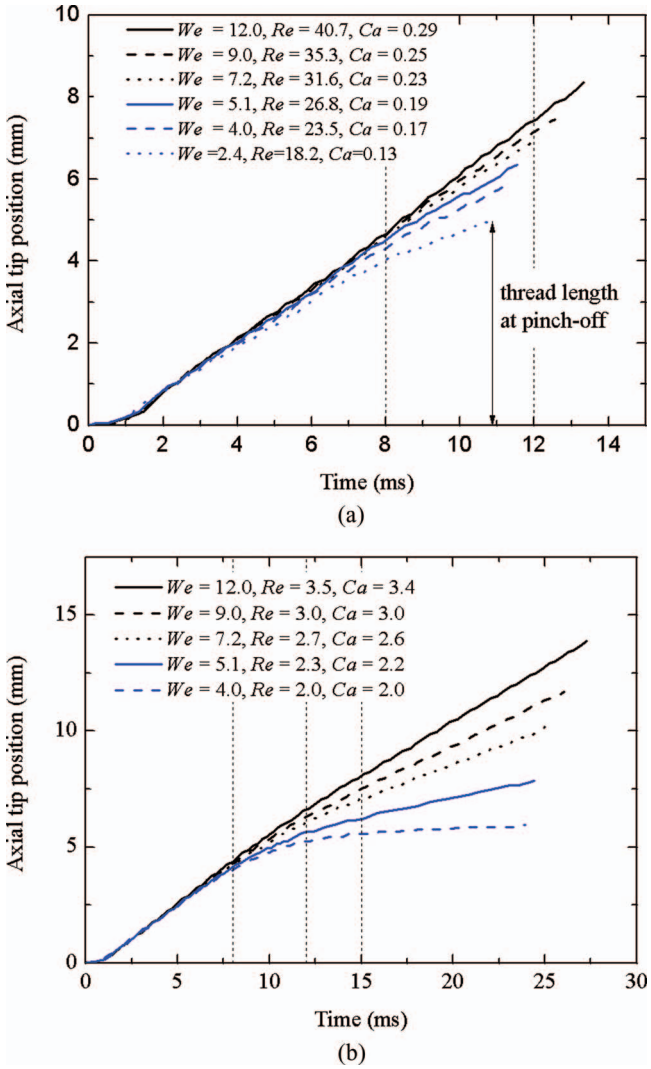

FIG. 3. Time evolution of axial tip position up to the pinch-off: (a) $Z = 11.8$ and (b) $Z = 1$.

and it can be used as a velocity scale for characterizing the inertial effects, which are induced by the actuation pulse. Therefore, the ejection speed ($\sim$0.6 ms^{-1}) during the initial stage was used for calculating the non-dimensional parameters such as the *Re*, *We*, and *Ca*.

After 4 ms, the ejection speed decreased as the viscosity and surface tension increased, as shown in Fig. 3. This can be explained by the relative importance of the inertial, capillary, and viscous forces. During the ejection and stretching of the liquid thread before pinch-off, inertial forces induced by the actuation pulse drive the forward ejection of the liquid thread, whereas the capillary and viscous forces tend to resist the forward ejection of the liquid thread.[16] Therefore, the ejection process is governed by the *Re* and *We*, which represent the ratios of inertial to viscous and inertial to surface tension forces, respectively. Both in Figs. 3(a) and 3(b), despite the identical *Z* number, the ejection speed was decreased as the values of the *Re* and *We* decreased because the resistance force against ejection was increased owing to the higher value of viscosity and surface tension. This indicates that the droplet ejection behavior is not only governed by the value of *Z* but also by the value of the *Re* and *We*.

2. Pinch-off time

The pinch-off time, at which the liquid thread separates from the nozzle, differed depending on the jetting conditions. In Figs. 3(a) and 3(b), the fluid with a lower *Ca* value showed a faster

pinch-off. This can be explained by the relative importance of the capillary and viscous forces. In the neck region, fluid flows out of the neck as it thins, by exiting upwards and downwards because a curvature-induced pressure increased there.[31] Therefore, during the necking process, capillary forces promote thinning of the neck, whereas the viscous forces tend to resist thinning of the neck. That is, the necking process was governed by the *Ca*, which represents the ratio of viscous to capillary forces; the necking process became faster as the *Ca* decreased.

The pinch-off times were between 11 and 14 ms at $Z = 11.8$, whereas they were between 25 and 28 ms at $Z = 1$, as shown in Figs. 3(a) and 3(b). The delayed pinch-off time is because of a much higher level of viscosity (i.e., a much lower *Z* number and much higher *Ca* number), which resists thinning of the neck. From a practical point of view, the pinch-off time is related to the droplet generation frequency, but we will not evaluate the pinch-off time with respect to the frequency.

3. Liquid thread length at pinch-off

The length of the liquid thread at pinch-off was influenced by both the ejection speed and pinch-off time. At a fixed *Z* number, the lower ejection speed resulting from a lower *We* and *Re* and the faster pinch-off resulting from a lower *Ca* lead to a shorter liquid thread length, as shown in Figs. 3(a) and 3(b). The liquid thread length is an important parameter because an increasing thread length usually leads to an increased risk of satellite droplet formation.

4. Recoil, satellite droplet formation, and recombination of satellite droplets with main droplets

After pinch-off, the tail retracts toward the head owing to high pressure in the tail tip,[6] forming a single sphere droplet. In some conditions, secondary pinch-off occurs, forming satellite droplets. The secondary pinch-off is influenced by both the tail length and *Ca* number. At a relatively longer tail length, capillary waves, which lead to multiple breakup,[6] were observed, as shown in Fig. 4(a). As the tail length decreased, satellite droplet formation was suppressed, as shown in Figs. 4(a)–4(c). For a larger *Ca*, the satellite formation could be suppressed because of higher viscous resistance in the secondary neck region. Despite Fig. 4(d) showing a longer thread length than that in Fig. 4(a), secondary pinch-off was not observed in Fig. 4(d) owing to a higher *Ca*, corresponding to a higher viscous resistance against a secondary necking process. Dong *et al.*[6] proposed the limit for liquid thread length without secondary pinch-off, but we do not discuss this quantitatively because it is beyond the scope of this paper.

Under certain conditions, the satellite droplet recombines with the primary droplet. The recombination of satellite droplets with the main droplet depends on the relative velocity of the satellite droplet and main droplet. When the velocity of the satellite droplet is higher than that of the main droplet, the satellite droplets merge with the main droplet.[6] Usually, the tiny satellite droplets that result from multiple breakup tend to merge with a following larger satellite droplet because smaller satellite droplets undergo a larger deceleration because of the drag force exerted on them by air.[6] This is also observed in Fig. 4(a), where small satellite droplets merge with the following satellite droplets instead of the main droplet. Dong *et al.*[6] suggested a necessary condition for a merger of a satellite droplet with the main droplet, but we do not discuss this quantitatively because it is beyond the scope of this paper.

B. Printability range

The previously discussed qualitative effects of the non-dimensional parameters revealed that the droplet formation dynamics could differ depending on the values of *Re*, *We*, and *Ca* despite having the same *Z* number. This indicates that the printability range should be determined taking into account the important parameters *Z*, *Re*, *We*, and *Ca*. To determine the printability range, further numerical simulations were carried out under a wide range of jetting conditions. The results of all the numerical simulations were used for constructing a regime map. In the present study, five regimes of droplet formation behavior were observed. The transition between the regimes was not investigated quantitatively; instead, a rough map for distinguishing the five different regimes is shown in Fig. 5.

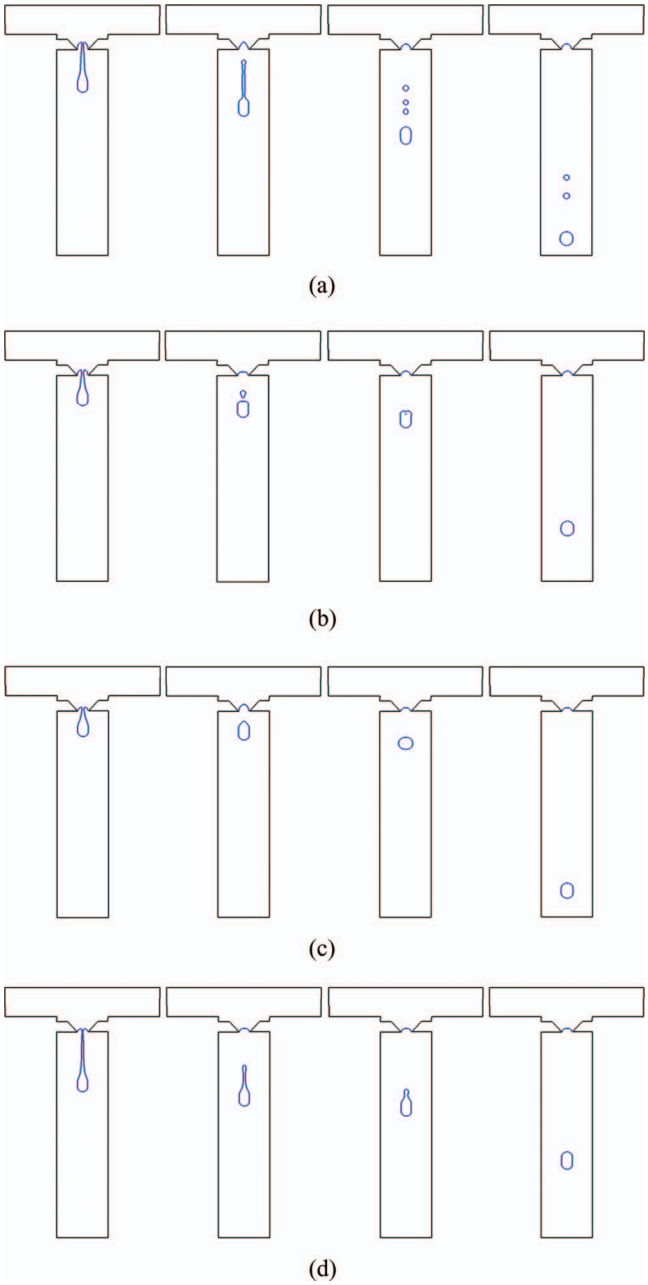

FIG. 4. Time evolution of droplet shape after the pinch-off: (a) $Z = 11.8$, $We = 12.0$, and $Ca = 0.29$ at $t = 13.3$, 20.4, 27.9, and 50.8 ms (Regime II); (b) $Z = 11.8$, $We = 4.0$, and $Ca = 0.17$ at $t = 11.2$, 16.5, 20.9, and 52.0 ms (Regime I); (c) $Z = 11.8$, $We = 2.4$, and $Ca = 0.13$ at $t = 10.8$, 13.7, 20.9, and 66.6 ms (Regime I); (d) $Z = 1$, $We = 9.0$, and $Ca = 3.0$ at $t = 26.1$, 32.9, 37.3, and 55.7 ms (Regime I).

The regime map in Fig. 5 could be a useful guide for selecting the jetting conditions in DOD inkjet printing (all the operating parameters used for the simulations and corresponding regime are listed in supplementary material[32]).

1. Regime I

This region indicates the printability region, within which a single droplet is formed. Jang *et al.*[25] observed droplet formation dynamics within a travel (falling) distance of $20D_n$, and they classified certain droplet formation dynamics as printable: absent of second pinch-off or recombination of

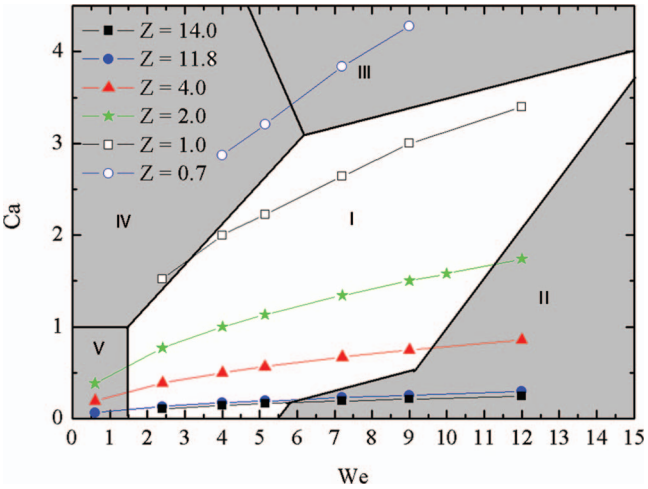

FIG. 5. Regime map dividing the droplet formation dynamics into five different regimes.

satellite droplets with the main droplet forming a single droplet, as shown in Figs. 4(b)–4(d). We also observed droplet formation dynamics within a travel distance of $20D_n$ and found the printable jetting conditions in terms of *We*, *Ca*, and *Z*. Although the jetting conditions have the same *Z* number, printability depended on the *We* and *Ca* values.

2. Regime II

At a relatively small *Ca* and large *We*, one or more satellite droplets are generated, but they do not recombine with the main droplet, as shown in Fig. 4(a). At a large *We*, relatively large inertial forces result in longer tail at pinch-off and a wave-like instability along the liquid thread leading to multiple breakup.[6] Multiple breakups generate smaller satellites which encounter larger deceleration in air leading to merging with the following satellite droplets instead of the main droplet.[6]

3. Regime III

At a large *Ca* and *We*, pinch-off occurs after a relatively longer pinch-off time, but very thin and long-lasting threads generate a fine satellite droplet, as shown in Fig. 6(a). The fine satellite droplet was not merged with the main droplet owing to a larger deceleration resulting from air drag,[6] as shown in Fig. 6(a).

4. Regime IV

At a large *Ca* (>1) and small *We*, inertial force is not strong enough to pinch off the liquid thread. In this regime, viscous forces dominate the capillary, therefore, the fluid fails to eject because the increased viscous force dissipates the inertial force required to eject the fluid out of the nozzle, as shown in Fig. 6(b).

5. Regime V

At a small *We* (<1) and *Ca* (<1), surface tensional forces dominate the inertial and viscous forces; therefore, the fluid fails to eject because the surface tensional forces resist fluid ejection, as shown in Fig. 6(c). Duineveld *et al.*[33] and Xu and Basaran[18] also reported that pinch-off does not occur when *We* is low.

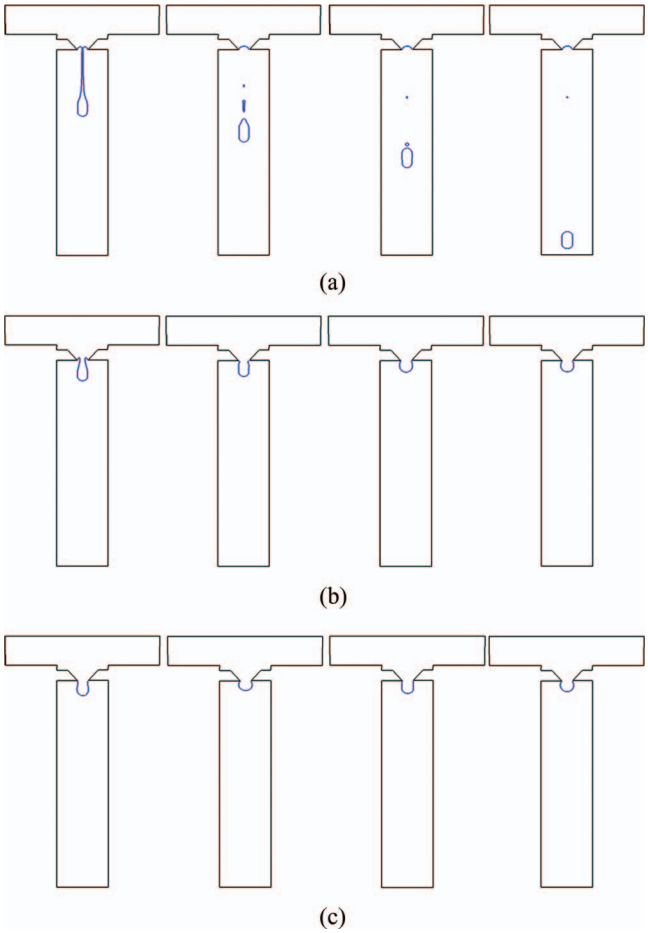

FIG. 6. Time evolution of droplet shape after the pinch-off: (a) $Z = 0.7$, $We = 9.0$, and $Ca = 4.3$ at $t = 34.7$, 47.7, 57.9, and 82.4 ms (Regime III); (b) $Z = 1$, $We = 2.4$, and $Ca = 1.5$ at $t = 14.1$, 18.5, 24.6, and 43.1 ms (Regime IV); and (c) $Z = 11.8$, $We = 0.6$, and $Ca = 0.07$ at $t = 10.3$, 14.0, 25.3, and 55.5 ms (Regime V).

IV. CONCLUSIONS

The DOD droplet formation dynamics was investigated by carrying out numerical simulations regarding the printability range, and the qualitative effects of non-dimensional parameters on the droplet formation dynamics were evaluated. At a fixed Z number, the ejection speed decreased as the Re and We decreased and the pinch-off occurs faster as the Ca decreased. The dynamics related to the satellite droplets also differed depending on the values of the Re, We, and Ca, even at a fixed Z number. The different droplet formation dynamics under different Re, We, and Ca values and at a fixed Z number indicated that the Z number alone was not sufficient for describing the droplet formation dynamics. Therefore, the printability range should be determined by taking into consideration the important parameters Re, We, and Ca as well as Z. Through extensive numerical simulations, a regime map in which the droplet formation dynamics are divided into five regimes was provided and the printability range was determined in a parameter space of the Z, We, and Ca. The obtained information is believed to provide a useful reference for selecting the appropriate jetting conditions in DOD inkjet printing.

[1] A. M. J. van den Berg, P. J. Smith, J. Perelaer, W. Schrof, S. Koltzenburg, and U. S. Schubert, "Inkjet printing of polyurethane colloidal suspensions," Soft Matter **3**, 238 (2007).
[2] J. Stringer and B. Derby, "Limits to feature size and resolution in ink jet printing," J. Eur. Ceram. Soc. **29**, 913 (2009).
[3] Y. Ishii, S. Koike, Y. Arai, and Y. Ando, "Ink jet fabrication of polymer microlens for optical-I/O chip packaging," Jpn. J. Appl. Phys. **39**, 1490 (2000).

[4] J. M. Lai, C. Y. Huang, C. H. Chen, K. Linliu, and J. D. Lin, "Influence of liquid hydrophobicity and nozzle passage curvature on microfluidic dynamics in a drop ejection process," J. Micromech. Microeng. **20**, 015033 (2010).
[5] A. U. Chen and O. A. Basaran, "A new method for significantly reducing drop radius without reducing nozzle radius in drop-on-demand drop production," Phys. Fluids **14**, L1 (2002).
[6] H. Dong, W. W. Carr, and J. F. Morris, "An experimental study of drop-on-demand drop formation," Phys. Fluids **18**, 072102 (2006).
[7] A. A. Goghari and S. Chandra, "Producing droplets smaller than the nozzle diameter by using a pneumatic drop-on-demand droplet generator," Exp. Fluids **44**, 105 (2008).
[8] J. R. Castrejón-Pita, G. D. Martin, S. D. Hoath, and I. M. Hutchings, "A simple large-scale droplet generator for studies of inkjet printing." Rev. Sci. Instrum. **79**, 075108 (2008).
[9] K. S. Kwon, "Experimental analysis of waveform effects on satellite and ligament behavior via *in situ* measurement of the drop-on-demand drop formation curve and the instantaneous jetting speed curve," J. Micromech. Microeng. **20**, 115005 (2010).
[10] P. Shin, J. Sung, and M. H. Lee, "Control of droplet formation for low viscosity fluid by double waveforms applied to a piezoelectric inkjet nozzle," Microelectron. Reliab. **51**, 797 (2011).
[11] X. Wang, W. W. Carr, D. G. Bucknall, and J. F. Morris, "Drop-on-demand drop formation of colloidal suspensions," Int. J. Multiphase Flow **38**, 17 (2012).
[12] J. E. Fromm, "Numerical-calculation of the fluid-dynamics of drop-on-demand jets," IBM J. Res. Dev. **28**, 322 (1984).
[13] R. L. Adams and J. Roy, "A one-dimensional numerical-model of a drop-on-demand ink jet," J. Appl. Mech. **53**, 193 (1986).
[14] T. W. Shield, D. B. Bogy, and F. E. Talke, "A numerical comparison of one-dimensional fluid jet models applied to drop-on-demand printing," J. Comput. Phys. **67**, 327 (1986).
[15] N. Reis and B. Derby, "Ink jet deposition of ceramic suspensions: Modeling and experiments of droplet formation," Mater. Res. Soc. Symp. Proc. **625**, 117 (2000).
[16] J. Q. Feng, "A general fluid dynamics analysis of drop ejection in drop-on-demand ink jet devices," J. Imaging Sci. Technol. **46**, 398 (2002).
[17] A. S. Yang, J. C. Yang, and M. C. Hong, "Droplet ejection study of a Picojet printhead," J. Micromech. Microeng. **16**, 180 (2006).
[18] Q. Xu and O. A. Basaran, "Computational analysis of drop-on-demand drop formation," Phys. Fluids **19**, 102111 (2007).
[19] T. M. Liou, C. Y. Chen, and K. C. Shih, "Effects of actuating waveform, ink property, and nozzle size on piezoelectrically driven inkjet droplets," Microfluid. Nanofluid. **8**, 575 (2010).
[20] H. Wijshoff, "The dynamics of the piezo inkjet printhead operation," Phys. Rep. **491**, 77 (2010).
[21] N. F. Morrison and O. G. Harlen, "Viscoelasticity in inkjet printing," Rheol. Acta **49**, 619 (2010).
[22] B. Derby, "Inkjet printing ceramics: From drops to solid," J. Eur. Ceram. Soc. **31**, 2543 (2011).
[23] B. Derby and N. Reis, "Inkjet printing of highly loaded particulate suspensions," MRS Bull. **28**, 815 (2003).
[24] R. M. Meixner, D. Cibis, K. Krueger, and H. Goebel, "Characterization of polymer inks for drop-on-demand printing systems," Microsyst. Technol. **14**, 1137 (2008).
[25] D. Jang, D. Kim, and J. Moon, "Influence of fluid physical properties on ink-jet printability," Langmuir **25**, 2629 (2009).
[26] N. Reis, C. Ainsley, and B. Derby, "Ink-jet delivery of particle suspensions by piezoelectric droplet ejectors," J. Appl. Phys. **97**, 094903 (2005).
[27] N. Link and R. Semiat, "Ink drop motion in wide-format printers: 1. Drop flow from drop-on-demand (DOD) printing heads," Chem. Eng. Process. **48**, 68 (2009).
[28] C. W. Hirt and B. D. Nichols, "Volume of fluid (VOF) method for the dynamics of free boundaries," J. Comput. Phys. **39**, 201 (1981).
[29] J. U. Brackbill, D. B. Kothe, and C. Zemach, "A continuum method for modeling surface tension," J. Comput. Phys. **100**, 335 (1992).
[30] J. R. Castrejón-Pita, N. F. Morrison, O. G. Harlen, G. Martin, and I. M. Hutchings, "Experiments and Lagrangian simulations on the formation of droplets in drop-on-demand mode," Phys. Rev. E **83**, 036306 (2011).
[31] M. R. Davidson and J. J. Cooper-White, "Pendant drop formation of shear-thinning and yield-stress fluids," Appl. Math. Model. **30**, 1392 (2006).
[32] See supplementary material at http://dx.doi.org/10.1063/1.4742913 for the tables with all the operating parameters used in this paper.
[33] P. C. Duineveld, M. A. de Kok, M. Buechel, A. H. Sempel, K. A. H. Mutsaers, P. van de Weijer, I. G. Camps, T. van de Biggelaar, J-E. j. Rubingh, and E. I. Haskal, "Ink-jet printing of polymer light-emitting devices," Proc. SPIE **4464**, 59–67 (2002).